Combustion and Flame 159 (2012) 181–193

Contents lists available at ScienceDirect

Combustion and Flame

journal homepage: www.elsevier.com/locate/combustflame

Soot predictions in premixed and non-premixed laminar flames using a sectional approach for PAHs and soot

Thomas Blacha *, Massimiliano Di Domenico, Peter Gerlinger, Manfred Aigner

DLR – German Aerospace Center, Pfaffenwaldring, 38-40, 70659 Stuttgart, Germany

ARTICLE INFO

Article history:
Received 5 April 2011
Received in revised form 4 July 2011
Accepted 12 July 2011
Available online 6 August 2011

Keywords:
Soot
PAH
Sectional approach
Finite-rate chemistry
Laminar flame
Enthalpy

ABSTRACT

A new soot model is presented, which has been developed for CFD applications, combining accuracy and efficiency. While the chemical reactions of small gas phase species are captured by a detailed chemical kinetic mechanism, polycyclic aromatic hydrocarbons (PAHs) and soot particles are represented by sectional approaches. The latter account for important mechanisms such as the formation of sections, their oxidation, the condensation of acetylene, and the collisions between sections. The model has been designed to predict soot for a variety of fuels with good accuracy at relatively low computational cost. Universal model parameters are applied, which require no tuning in dependence of test case or fuel. Soot predictions of ethylene, propylene, kerosene surrogate, and toluene flames are presented, which show good agreement with the experimental data. Furthermore, the importance of the correct choice for thermodynamic data of PAHs and soot is highlighted and the impact of heat radiation is discussed.

1. Introduction

Soot can be found in a variety of combustion applications despite the fact that it is known to be an important pollutant. Not only does it affect the environment but also human health [1–4]. In addition, it may cause technical problems such as locally elevated heat loads for the combustor walls due to heat radiation [5–7]. Although soot has been studied over the last decades by a variety of research groups, it is still far from being completely understood [8]. During combustion of hydrocarbons it is formed in fuel-rich regions of the flame within a given temperature range. However, fuel rich conditions are very difficult to avoid, especially in the case of liquid fuels. Hence, it is important to better understand soot formation and the involved chemical processes in order to decrease soot emissions in practical applications.

Various soot models have been published in the past. The simplest among them are empirical models, which are usually restricted to the choice of fuel and to specific operating conditions. Nevertheless, once correctly tuned, they allow sensitivity analyses at low computational cost [9,10].

Semi-empirical models include PAH and soot chemistry in a simplified way. Their chemical mechanisms take major soot growth species such as acetylene or even aromatics into account. The flamelet approach, for example, where species concentrations are linked to scalars such as mixture fraction, allows reasonable predictions in non-premixed flames [11–14]. However, in combustion systems where premixing effects and strong turbulence-chemistry interactions are involved the applicability of this approach is limited.

More analytical but computationally expensive methods use detailed finite-rate chemistry for molecular species, while soot particles are lumped in one way or another. For the interface between gas phase and soot different techniques exist. While in simplified models soot is directly formed from acetylene [11,12,15–17], more detailed models use aromatic species such as benzene [18,19], naphthalene [20], or even pyrene [21,22].

One of the most basic ways of lumping soot is found in two equation soot models, where soot is represented by two variables only, e.g. soot mass fraction and soot number density [16,19,23–26]. Although these models contain no information about the soot size distribution, they allow predictions in soot volume fraction, number density, and mean particle size. Depending on the underlying chemical mechanism, promising CFD results have been achieved in the past with these models even for complex 3D configurations [27,28].

A more detailed lumping technique is the method of moments [15,29,30]. Here the soot size distribution is described by its moments, for which transport equations are solved. Although the correct description of the physical size distribution function includes an infinite number of moments, the moments of most interest are usually only those of low order [31–33]. Moreover, assuming a logarithmic size distribution, already the first three moments suffice for a complete description [34]. But this assumption is not generally valid [35–39]. Instead, a priori information about the

* Corresponding author. Fax: +49 711 6862 578.
E-mail addresses: Thomas.Blacha@dlr.de (T. Blacha), Massimiliano.Didomenico@dlr.de (M. Di Domenico), Peter.Gerlinger@dlr.de (P. Gerlinger).

0010-2180/$ - see front matter © 2011 The Combustion Institute. Published by Elsevier Inc. All rights reserved.
doi:10.1016/j.combustflame.2011.07.006

Nomenclature

A	surface area	T	temperature
c	stoichiometric coefficient	T_a	activation temperature
C	concentration	u	axial velocity
d	diameter	Y	mass fraction
fv	soot volume fraction	α	exponent of Arrhenius reaction rate
k	Arrhenius reaction rate	β	collision frequency
k_0	constant of Arrhenius reaction rate	η	oxidation efficiency
k_B	Boltzmann constant	ϕ	premixing ratio
m	mass	γ	collision efficiency
M	molecular mass	ν	stoich. coeff.: forward (') and backward ('')
N_a	Avogadro constant	ρ	density
N_r	number of reactions		
N_{sp}	number of species	*sub- and superscripts*	
O'	reaction order of educt	i, j, k	general index for sections
S_α	chemical source term of species α	s	soot
S_r	chemical source from reaction r	α, β	general species index

shape of the distribution function is needed in order to determine the required number of moments.

One of the most detailed lumping techniques is the sectional approach [20–22,40,41]. Here soot particles are lumped into sections, which are then treated as "virtual" species with averaged properties. The great advantage of this technique is that any kind of size distribution can be captured and that different sized particles may have different properties like reactivity, for example. Furthermore, sections can be treated in analogy to real species in many regards. Especially in combination with other models, such as heat radiation or turbulence chemistry interaction, this analogy is a great advantage as far as the effort of implementation is concerned. However, such methods are mostly applied to rather simple test cases like laminar flames because the involved computational effort is usually relatively high.

Particle tracking techniques [35,42], where soot particles are not lumped by properties but by number, may reach an even higher degree of detail depending on the number of stochastic particles used.

The model described in this work features a sectional approach, so that soot size distributions can be predicted at any point of the flame without a priori knowledge of the shape of the distribution function. In order to reduce the computational effort, PAH molecules are also captured by a sectional approach. Furthermore, PAH and soot sections with radical branches are not treated separately, resulting in a skeletal global reaction formulation.

The model is applied to a variety of fuels and flames showing its capability to predict soot with good accuracy at acceptable computational cost without the need of any tuning. With respect to the combination of accuracy and efficiency, this model bridges the gap between very detailed and computationally low cost models. In this regard, it is not the purpose of this work to show higher accuracy than very detailed soot models when applied to laminar flames but to significantly reduce the computational cost in order to be able to calculate more complex test cases.

2. Numerical model

All presented results have been obtained by means of steady state simulations using the DLR in-house Code THETA – an incompressible flow solver for finite-volume grids, which has been optimized for combustion problems. It features a multigrid algorithm, dual grid technique, a stiff-chemistry solver, and parallelization via domain decomposition.

The soot model consist of three sub models describing molecular gas phase species, polycyclic aromatic hydrocarbons (PAHs), and soot. In order to improve the compatibility with other models and to reduce the computational cost, the chemical source term is represented in a global Arrhenius like formulation in all sub models

$$S_\alpha = M_\alpha \sum_{r=1}^{N_r} \left(\nu''_{\alpha,r} - \nu'_{\alpha,r}\right) S_r. \tag{1}$$

with

$$S_r = k_0 T^\alpha exp(-T_a/T) \prod_{\beta=1}^{N_{sp}} C_\beta^{O'_{\beta,r}}. \tag{2}$$

All sub models respect mass conservation also regarding their interaction.

2.1. Gas phase chemistry

The chemical kinetic mechanism of the gas phase consists of the base mechanism mentioned in [43], which has mainly been derived from the works by Slavinskaya et al. [44,45]. It considers molecular species up to the first aromatic ring including benzene, toluene, and their radicals. For the kerosene surrogate flame, consisting of volumetric 12% toluene (C_7H_8), 23% isooctane (C_8H_{18}), and 65% *n*-decane ($C_{10}H_{22}$), a sub mechanism is added, which has been derived from another work by Slavinskaya et al. [46], where this surrogate has first been proposed.

The base mechanism as well as the kerosene surrogate sub mechanisms have already extensively been validated in the past by different authors [43,47,46]. The conjunction of the two mechanisms has been validated for ignition delay with respect to Jet A-1 fuel.

2.2. PAH chemistry

All aromatic molecules with a molecular mass between 100 and 800 g/mol are considered PAHs (Polycyclic Aromatic Hydrocarbons). They are represented by three logarithmically spaced PAH sections with a scaling factor of two as demonstrated in Fig. 1. For reasons of computational efficiency, radical PAHs are not considered separately but a global formulation is chosen.

During the current work the intra sectional mass distribution function, describing the mass distribution within one PAH section,

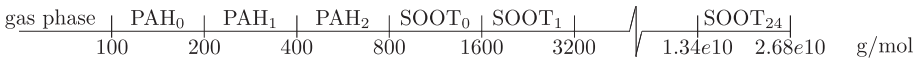

Fig. 1. PAH and soot distribution.

is assumed to be constant in particle number density. For analyzing purposes a mass distribution function being constant in mass is also supported. Based on the distribution function the calculation of mean molecular masses and stoichiometric coefficients is straightforward. An example can be found in the work by Pope and Howard [48]. The impact of the choice of distribution function on mean molecular masses, stoichiometric coefficients, or soot predictions has already been discussed elsewhere [23,43,48]. Species specific data such as H/C ratio or enthalpy values are inter- and extrapolated from 43 reference PAHs taken from the work by Yu et al. [49] (see Figs. 2 and 3). These are six ring PAHs, ranging from benzene up to tetrabenzoperylene. Transport properties have been obtained using a similar procedure with data by Richter et al. [21]. The authors are aware that thermodynamic data of same sized PAHs may differ but this data is only used to calculate mixture properties. Since in the considered test cases PAH concentrations are rather small, an error originating from the fitting procedure has only little effect on the mixture. In contrast, backward reaction rates should not be calculated based on the fitted data because in this case the error amplifies exponentially.

PAH chemistry is divided into four sub mechanisms, namely PAH_0 gas phase interaction, C_2H_2 condensation, PAH collision, and PAH oxidation reactions.

PAH_0 gas phase interactions consider all reactions of the gas phase with the first PAH section, PAH_0, including oxidation. In the current work 19 reversible reactions have been used, which are summarized in Table 1. These reactions have been derived from the detailed kinetic mechanisms by Slavinskaya and Frank [45] and Richter et al. [21], describing polycyclic aromatic growth from benzene, toluene, and their radicals. Reversible reactions are used at this point in order to capture the high reversibility of PAH formation reactions. Reverse reaction rates have been calculated based on the original reactions before lumping. In order to meet mass conservation, stoichiometric coefficients need to be added to the PAH_0 side as a function of its mean molecular mass.

All further sub models of PAH chemistry have been derived from the work by Di Domenico et al. [19,50] and were enhanced in several aspects. Since the H/C ratio diminishes for growing PAHs, hydrogen abstraction is included in growth reactions in order to fulfill atom conservation. Furthermore, instead of only accounting for same sized PAH collisions, now, all PAH sections may collide with one another. Stoichiometric coefficients are no longer calculated based on approximated ratios but depending on the intra sectional distribution function and atom conservation. All mass source terms beyond the upper bound of the PAH range are fed to the first soot species while source terms at the lower bound have already been accounted for by the PAH_0 gas phase interaction model.

Consequently, PAH growth via C_2H_2 condensation reads

$$PAH_i + C_2H_2 \rightarrow c_1 PAH_i + c_2 PAH_{i+1} + c_3 H_2 \quad (3)$$

representing a global formulation of the well-known HACA mechanism [51,52]. For the last PAH section this reaction leads to the first soot section $SOOT_0$ instead of PAH_{i+1}. Although the authors are aware of the reversibility of PAH growth reactions [53], this mechanism is regarded irreversible due to the high uncertainty of backward reaction rates. However, the reversible character of PAH growth has at least partially been captured by the PAH_0 gas phase interaction model mentioned above.

With $j \leqslant i$ the PAH collision model reads

$$PAH_i + PAH_j \rightarrow c_1 PAH_i + c_2 PAH_{i+1} + c_3 H_2. \quad (4)$$

Again this reaction leads to soot instead of PAH_{i+1} in case $i = 2$.

Although it is known that for small PAH the backward reaction rate of Eq. (4) may become important, this reaction has been

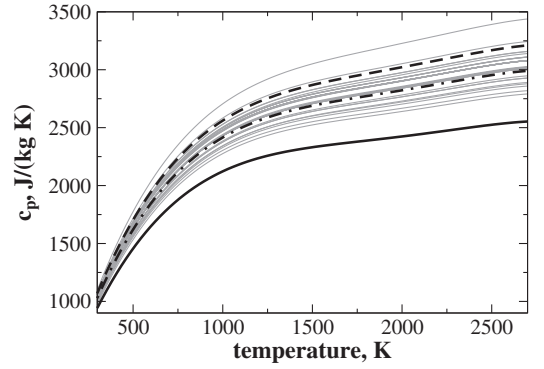

Fig. 2. Inter- and extrapolation of the mass specific heat capacity. Reference PAHs (thin gray), PAH_0 (black dash), PAH_1 (black dash dot), PAH_2 (black solid).

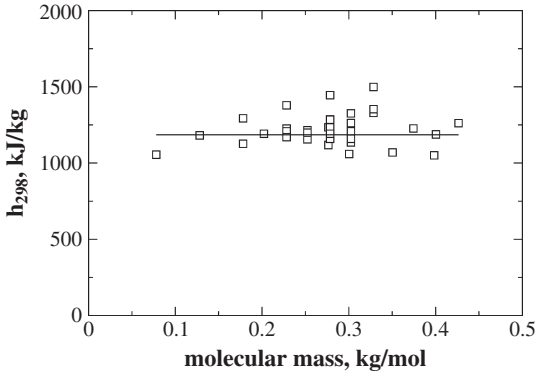

Fig. 3. Averaging of the mass specific enthalpy of formation. The average value from reference PAHs (symbols) is used for PAH_0–PAH_2 (line).

Table 1
PAH_0 gas phase interaction reactions. Units are mol, cm, s, and K.

	k_0	α	T_a
$A_1^- + C_2H_4 = PAH_0 + H$	2.51E+12	0.00	3095.00
$A_1^- + C_3H_4 = PAH_0 + H$	1.00E+16	0.00	16600.00
$A_1^- + C_3H_3 = PAH_0$	6.46E+12	0.00	0.00
$A_1^- + C_4H_2 = PAH_0 + C_2H$	2.00E+11	0.00	0.00
$A_1 + C_2H = PAH_0 + H$	1.00E+12	0.00	0.00
$A_1 + C_2H_3 = PAH_0 + H$	7.90E+11	0.00	3200.00
$A_1 + A_1^- = PAH_0 + H$	1.10E+23	−2.92	7450.00
$A_1 + A_1^- = PAH_0$	2.000e+26	−3.90	3180.344
$C_7H_7 + CH_2 = PAH_0 + H$	2.40E+14	0.00	0.00
$C_7H_7 + C_3H_3 = PAH_0 + 2H$	6.00E+11	0.00	0.00
$C_7H_7 + C_2H_2 = PAH_0 + H$	3.200e+11	0.00	3522.53
$PAH_0 + H = A_1^- + C_2H_2$	2.00E+14	0.00	4882.00
$PAH_0 + O = A_1^- + HCCO$	2.10E+07	2.00	950.00
$PAH_0 + O = A_1^- + CH_3 + CO$	1.92E+07	1.83	110.00
$PAH_0 + O = C_7H_7 + HCCO$	2.00E+13	0.00	2000.00
$PAH_0 + OH = A_1^- + CH_2CO$	2.18E−04	4.50	−500.00
$PAH_0 + OH = A_1 + HCCO$	2.44E+03	3.02	5574.00
$PAH_0 + OH = C_7H_7 + CH_2O$	1.40E+12	0.00	0.00
$PAH_0 + OH = C_7H_7 + CH_2CO$	1.00E+13	0.00	5000.00

modeled irreversible due to the high uncertainty of the backward reaction rates. The Arrhenius reaction rate for the forward reaction can be written

$$k = 2.2 N_a \gamma_{i,j} \beta_{i,j} \tag{5}$$

with 2.2 being the average van der Waals enhancement factor according to Harris and Kennedy [54] and Miller [55]. N_a is the Avogadro constant, $\gamma_{i,j}$ the collision efficiency, and $\beta_{i,j}$ the collision frequency. For $\gamma_{i,j}$ a constant value of 0.3 was chosen [19] while for $\beta_{i,j}$ a general calculation procedure has been implemented in THETA using the equations mentioned by Fuchs [56]. In his work a general formulation of collision frequencies is given for all Knudsen numbers. Since this formulation is rather complex, the resulting reaction rate has been fitted to Arrhenius parameters in a preprocessing step using the least square method. The approach of a blending function between continuum and free molecular regime afore mentioned by El-Asrag and Menon [57] or by Hu [58] is not used because it is less accurate and the advantage of lower computational cost is irrelevant as the preprocessing calculations require only seconds.

The fitting error in the whole Knudsen number range is always smaller than 5% and disappears for the free molecular regime because here

$$\beta_{i,j} = \underbrace{\left(\frac{\pi k_B (m_i + m_j)}{2 m_i m_j}\right)^{0.5} (d_i + d_j)^2}_{k_0^*} T^{0.5}, \tag{6}$$

holds [40,59,55], which is already in Arrhenius formulation ($k_0 = 2.2 N_a \gamma_{i,j} k_0^*$, $\alpha = 0.5$, and $T_a = 0$). For the test cases discussed in this paper, the Knudsen number is always greater than one for PAH–PAH collisions and therefore the calculated collision frequencies are identical to Eq. (6).

The PAH oxidation mechanism takes O_2 and OH oxidation into account by the reactions

$$PAH_i + O_2 \rightarrow c_1 PAH_{i-1} + c_2 PAH_i + c_3 H_2 + 2CO, \tag{7}$$

$$PAH_i + OH \rightarrow c_1 PAH_{i-1} + c_2 PAH_i + c_3 H_2 + CO. \tag{8}$$

For $i = 0$ it follows that $c_1 = 0$ because PAH_0 oxidation leading to molecular species has already been captured by the PAH_0 gas phase interaction model.

All Arrhenius coefficients of the discussed PAH sub models are summarized in Table 2.

2.3. Soot chemistry

The soot model accounts for all species heavier than the last PAH species and makes use of a sectional approach, as well. All sections are logarithmically spaced with a default spacing factor of two as shown in Fig. 1. In order to reduce the computational cost, radicals are not treated separately, which yields a global representation of soot reactions. The default number of soot sections is 25 leading to a maximum possible particle weight of 2.7×10^{10} amu.

For the H/C ratio of soot particles the distribution mentioned by Richter et al. [21] has been fitted to a function of particle mass as given in Eq. (9). It is needed in order to correctly predict the stoichiometric coefficients for a matter of element conservation.

$$H/C = 0.4405 M^{-0.10524} \tag{9}$$

Patterson and Kraft [60] studied the impact of different aggregate structures of soot particles. Deviations in soot predictions were found, comparing the spherical particle model and models which conserve surface area during coagulation. A detailed consideration of different aggregate structures in a sectional model can be realized by solving two transport equations per section as done by Dworkin et al. [22]. Assuming spherical primary particles, they solved equations for primary particle number density and for soot aggregate density. Consequently, twice the number of transport equations are necessary for the soot model, which significantly increases the computational effort. But since promising results have been obtained in the past also without the consideration of aggregate structures [20,21,41], different particle shapes are not accounted for in favor of computational time savings. Therefore, all particles are assumed to be spherical with a density of 1800 kg/m^3.

In analogy to the PAH model the intra sectional mass distribution function is assumed to be constant in particle number density by default but distribution functions constant in mass are also supported and may be different from the distribution function used for PAH sections.

Using a numerical method where transport equations are solved for any kind of energy (usually enthalpy) and temperatures are calculated subsequently from it, soot enthalpy values should be defined with care. Very little data about soot enthalpies exist in the literature especially for small soot particles. The simplest approach in this regard is to neglect soot in the calculation of the mixture enthalpy [61]. This is identical to assuming that soot enthalpies equal zero. However, in strongly sooting flames this assumption may lead to an unphysical temperature rise because the mass transforming to soot will loose all of its enthalpy to the environment. As soot mainly consists of carbon, it may seem appropriate to use the thermodynamic properties of amorphous carbon but this approach is limited, too, because young soot also contains an important amount of hydrogen. Furthermore chemical bonds within soot particles may differ strongly from those found in amorphous carbon. Another common approach is to use the mass specific enthalpy values of some fundamental PAH species (usually the last PAH of the mechanism), since soot is formed from PAHs [20,21]. However, also this assumption is limited and may introduce significant errors in the calculation of the flame temperature. Due to these uncertainties we decided to define thermodynamic properties of soot in a way that they do not significantly alter the flame temperature. In consequence, the mass specific enthalpy values of the major soot growth species, acetylene, have been applied.

Figure 4 shows the impact of the choice of soot enthalpy on the temperature in a fuel-rich ethylene/air mixture with $\phi = 4$ in an isobaric adiabatic perfectly stirred reactor auto-igniting at an initial temperature of $T = 1200$ K at atmospheric pressure. Heat radiation is neglected, because in this example we only want to focus on the transfer of chemical energy. Plotted are temperatures and soot volume fractions versus time calculated with and without soot model. We notice that the zero enthalpy approach yields an important temperature rise of roughly 300 K compared to the simulation without soot model. The higher temperature in turn lowers the overall soot production. Furthermore, it can be observed that the rise in temperature occurs already at soot concentrations below 1 ppm, which is not unusually high for conventional atmospheric pressure flames. The thermodynamic data of the last PAH also leads to a temperature rise but it is difficult to judge at which extent this rise is physical or not because soot growth reactions may also be exothermic [62]. The temperature rise caused by

Table 2
Arrhenius parameters of the PAH model taken from Di Domenico et al. [19]. Units are mol, cm, s, and K.

	k_0	α	T_a
PAH–C_2H_2 growth	3.98E+07	0.0	5100
PAH–PAH collision	0.66 N_a k_0^*	0.5	0
PAH-oxidation			
O_2	2.0E+06	0.0	3800
OH	2.1E+07	0.0	2300

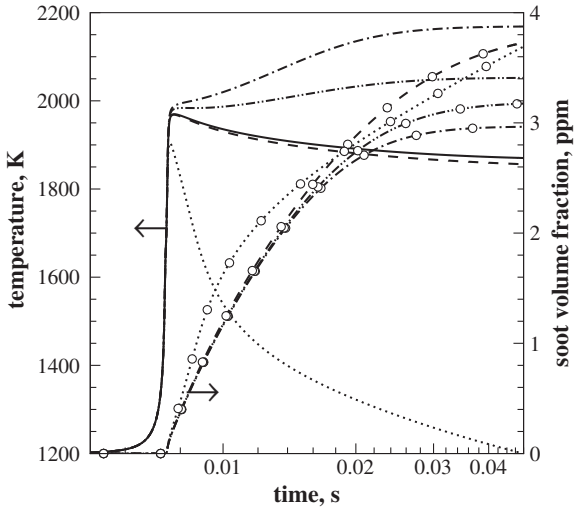

Fig. 4. Influence of soot enthalpy on temperature. Lines without symbols for temperature and with symbols for soot volume fraction: no soot (solid), $h_s = 0$ (dash dot), $h_s = h_{PAH_2}$ (dash dot dot), $h_s = h_{C_2H_2}$ (dash), and $h_s = h_C$ (dot).

soot formation disappears if the mass specific enthalpy of acetylene is used. Since now the bulk of mass transforming to soot has the same enthalpy as the major soot growth species, the slight deviations from the calculation without soot model are due to hydrogen abstraction, oxidation and the contribution of aromatics. The thermodynamic data of amorphous carbon (taken from Burcat's data base [63]) in contrast yields a very strong drop of the temperature with final temperatures as little as the initial temperature of the combustion process. Similar trends resulting from these approaches can be observed with any other hydrocarbon fuel which is supported by the model. The wide range of possible temperatures demonstrates the high uncertainties regarding thermodynamic data of soot particles and the strong need for reliable experimental data.

While molecular diffusion is considered for PAHs, it is neglected for soot. Instead thermophoresis is taken into account, which causes small aerosol particles (like soot) to follow a drift velocity against the temperature gradient. The drift velocity is independent of particle size [64,65] and for the free molecular regime it can be derived that

$$v_{th} \approx -0.55\ \nu\ \nabla T/T, \tag{10}$$

which is applicable up to the transition regime ($Kn \approx 1$) [66]. In the continuum regime ($Kn < 1$) though, the thermophoretic velocity strongly depends on the ratio of heat conductivities of the surrounding gas to the one of the particle [65]. The latter one is uncertain in the case of soot. However, since common thermophoresis-sensitive test cases (that we want to consider) are usually in the free molecular or the transition regime, v_{th} is calculated according to Eq. (10).

Heat radiation from soot is captured with the assumption of an optically thin medium according to Di Domenico et al. [19]. This approach accounts only for heat emission, while heat adsorption is neglected. Since soot is only found in small regions of the flame, radiated heat is unlikely to be reabsorbed, justifying the approach. More accurate radiation models exist, such as the spherical harmonics method, the discrete ordinates method, or the Monte Carlo method [67–69]. However, the radiation model used is by far the most cost-efficient one because it requires only a simple additional source term in the energy equation. In this regard, Liu et al. [70] compared temperature and soot predictions of a laminar ethylene diffusion flame using different heat radiation models. The deviation between the approach of the optically thin medium and the discrete-ordinates used in their work was found to be small for the case studied.

Soot chemistry is modeled using four different mechanisms, which have been derived from the work by Di Domenico et al. [19], namely soot growth via condensation of C_2H_2, soot growth via collisions with PAH molecules, soot coagulation, and soot oxidation. The formation of the first soot section $SOOT_0$ has already been captured by the PAH chemistry model. In analogy to the PAH chemistry, stoichiometric coefficients are determined based on the intra sectional mass distribution function and the H/C ratio given in Eq. (9).

The model for soot growth via condensation of C_2H_2 reads

$$SOOT_i + C_2H_2 \rightarrow c_1 SOOT_i + c_2 SOOT_{i+1} + c_3 H_2. \tag{11}$$

With the corresponding reaction source term

$$S_r = k_0 T^{\alpha} exp(-T_a/T) A_i^s [C_2H_2] \tag{12}$$

and

$$A_i^s = \pi N_a d_i^2 [SOOT_i] \tag{13}$$

follows

$$k_{0,i} = k_0 \pi N_a d_i^2 \tag{14}$$

to give the general expression mentioned in Eq. (2).

Soot growth via PAH collision can be written

$$SOOT_i + PAH_k \rightarrow c_1 SOOT_i + c_2 SOOT_{i+1} + c_3 H_2, \tag{15}$$

with

$$S_r = 2.2 \gamma_{i,k} \beta_{i,k} N_a [SOOT_i][PAH_k] \tag{16}$$

in analogy to Eq. (5). For the collision efficiency $\gamma_{i,k}$ a constant value of 0.3 was chosen as in the previous work by Di Domenico et al. [19]. D'Anna and Kent [20] suggested a possibility to estimate collision efficiencies for soot particles as a result of attractive and repulsive van der Waals forces, which can be described by the Lennard–Jones 6–12 intermolecular potential. Nevertheless, there are still uncertainties to this approach, in particular in conjunction with a simplified sectional model which does not treat radicals separately. Moreover, in the past, other authors [40,21] obtained reasonable results with constant collision efficiencies as well. As far as the calculation of the collision frequency $\beta_{i,k}$ is concerned, the same procedure has been used as mentioned in Section 2.2 for PAHs.

With $j \leqslant i$ the global reaction for soot coagulation can be written as follows

$$SOOT_i + SOOT_j \rightarrow c_1 SOOT_i + c_2 SOOT_{i+1} + c_3 H_2 \tag{17}$$

with

$$S_r = 2.2 \gamma_{i,j} \beta_{i,j} N_a [SOOT_i][SOOT_j]. \tag{18}$$

Since soot particles are rather big, it is assumed that every collision leads to coagulation. For the collision efficiency of soot particles $\gamma_{i,j}$ in Eq. (18) this assumption yields a constant value of 1. Arrhenius reaction rates can then be calculated in direct analogy to the PAH–soot collision model.

Finally, the soot oxidation model is described by the equations

$$SOOT_i + O_2 \rightarrow c_1 SOOT_{i-1} + c_2 SOOT_i + c_3 H_2 + 2CO, \tag{19}$$

$$SOOT_i + OH \rightarrow c_1 SOOT_{i-1} + c_2 SOOT_i + c_3 H_2 + CO, \tag{20}$$

with

$$S_r^{OX} = \eta^{OX} k_0^{OX} T^{\alpha^{OX}} exp\left(-T_a^{OX}/T\right) A_i^s [OX]. \tag{21}$$

Table 3
Arrhenius parameters of the soot sub mechanisms derived from Di Domenico et al. [19]. Units are mol, cm, s, and K.

	k_0	α	T_a
Soot – C_2H_2 growth	$350\pi N_a d_i^2$	0.0	12100
Soot – O_2 oxidation	$742\pi N_a d_i^2$	0.5	19800
Soot – OH oxidation	$1.15\pi N_a d_i^2$	0.5	0

Table 4
Summary of chemical mechanism.

	Standard		Kerosene sur.	
	Species	Reactions	Species	Reactions
Base mechanism	43	304	43	304
Kerosene sub mechanism	–	–	16	68
Soot and PAH model	28	499	28	499
Total	71	803	87	871

Here, *OX* may stand for either O_2 or OH. Together with Eq. (13) this yields

$$k_{0,i}^{OX} = \eta^{OX} k_0^{OX} \pi N_a d_i^2, \tag{22}$$

where η^{OX} represents the oxidation efficiency with values of 1.0 and 0.13 for O_2 and OH, respectively [19].

In Table 3 Arrhenius parameters are given for those models where a universal expression exists.

The dimensions of the resulting overall mechanism are shown in Table 4. The bulk of PAH and soot reactions is due to soot coagulation because every soot section may collide with every other. As a result, a reduction of soot sections can significantly reduce the number of global reactions. For example, 20 soot sections instead of 25 will reduce the number of global reactions to 359, which is adequate for most weekly sooting flames with maximum soot volume fractions around 1 ppm. However, in the present work 25 sections have been used for all test cases as a matter of generality.

3. Results and discussion

In this section model predictions for different laminar test cases will be discussed. Among these are zero-dimensional test cases, premixed one-dimensional flames, non-premixed axisymmetric flames, and partially premixed axisymmetric flames.

3.1. Predictions of Particle Size Distributions

Manzello et al. [71] studied PAH growth and soot inception in a well-stirred reactor (WSR) followed by a plug flow reactor (PFR). Air was supplied at a constant flow rate of 175 SLPM and ethylene (C_2H_4) fuel was fed to the WSR at equivalence ratios of ϕ = 1.8, 1.9, 2.0, and 2.1 with an uncertainty of $\Delta\phi$ = ±3%. The temperature of the PFR was on the order of 1400 K. For the WSR section only measurements for ϕ = 2.0 are reported (T = 1723 K) with uncertainties in temperature measurements of ±10%. Soot particle size distributions were measured using a dilution probe at the bottom most sampling port of the PFR.

For the calculations perfect mixing in the WSR and PFR is assumed and effects of the flow field are neglected. Thus, both reactors can be represented by two perfectly stirred isothermal reactors at atmospheric pressure. Residence times inside the reactors are 11 and 18 ms for WSR and PFR, respectively. One of the greatest uncertainties for the simulation is the choice of initial temperature of the WSR as demonstrated by Blacha et al. [43]. Bhatt and Lindstedt [72] suggested to use estimates from laminar flame calculations with temperature corrections resulting in temperatures of 1803, 1763, 1723, and 1823 K for ϕ = 1.8, 1.9, 2.0, and 2.1, respectively. For the present work temperature ranges were analyzed using Bhatt's values with a deviation of ±5%. Initial temperatures resulting in best agreement with the experiment are summarized in Table 5.

Table 5
Initial temperatures used for the WSR simulation. Units are K.

	ϕ = 1.8	ϕ = 1.9	ϕ = 2.0	ϕ = 2.1
Temperature	1803	1850	1810	1823

In Fig. 5 calculated soot size distributions are compared with the experimental data. While for ϕ = 1.8 the model fails to reproduce the measurements, good agreement is found for ϕ = 1.9, 2.0, and 2.1. The reason for the difficulties of the model at ϕ = 1.8 is mainly due to the fact that this condition is very close to the sooting limit, which in general represents a big challenge to predict. This drawback should be kept in mind for future model improvements.

The sensitivity of the model to the choice of intra sectional distribution function has also been investigated. As mentioned before, the intra sectional distribution function directly affects the mean molecular mass of a section as well as stoichiometric coefficients. Hence, reaction rates are affected, too. However, for the current test case the impact is negligible as shown in Fig. 5.

Since the measurements were restricted to a minimum diameter of approximately 3 nm, the local minimum of the soot size distributions in the region of very small soot particles could not be resolved experimentally. However, Zhao et al. [38,39] observed similar size distributions with local minima in the region of very small particles in laminar premixed ethylene flames. Singh et al. [37] explained that the minimum of bimodal soot particle distribution functions may be caused by the competition of soot inception and coagulation. According to our model this mechanism is also prevailing in the current test case as shown in Fig. 6. Here the size distribution resulting from the full model is compared to those obtained by excluding specific soot sub models inside the PFR. A simulation without soot oxidation has not been included in the graph because its impact is negligible. Also the impact of C_2H_2 condensation and coagulation with PAHs is very small, showing little effect on the general shape of the distribution. In contrast, coagulation reactions, which consume small particles to form bigger ones, cause a decline and a shift of the size distribution to the right. At the same time, soot formation leads to a strong rise in the number of small particles because new soot particles are continuously formed due to the fuel rich conditions. Therefore, in concordance with Singh et al. [37], the local minimum is a result of the concurrence of soot formation and coagulation reactions – one promoting small and the other big particles.

3.2. Laminar premixed ethylene, propylene, and toluene flames

Tsurikov et al. [73] studied laminar premixed flames at pressures between 1 and 5 bar for ethylene (C_2H_4), propylene (C_3H_6), and toluene (C_7H_8) using a water cooled flat flame burner. In order to reduce oxidation and heat losses at the edges of the flame, a shielding non-sooting flame surrounded the sooting one. Temperature measurements have been conducted using SV-CARS and soot volume fractions have been determined by LII. Reported uncertainties for temperature and soot volume fraction are ±3% and ±30%, respectively. All measurements are considered to only depend on the height above the burner, showing negligible gradients in radial direction. Therefore, calculations could be performed in one-dimensional space. The grid consisted of 600 hexahedrons

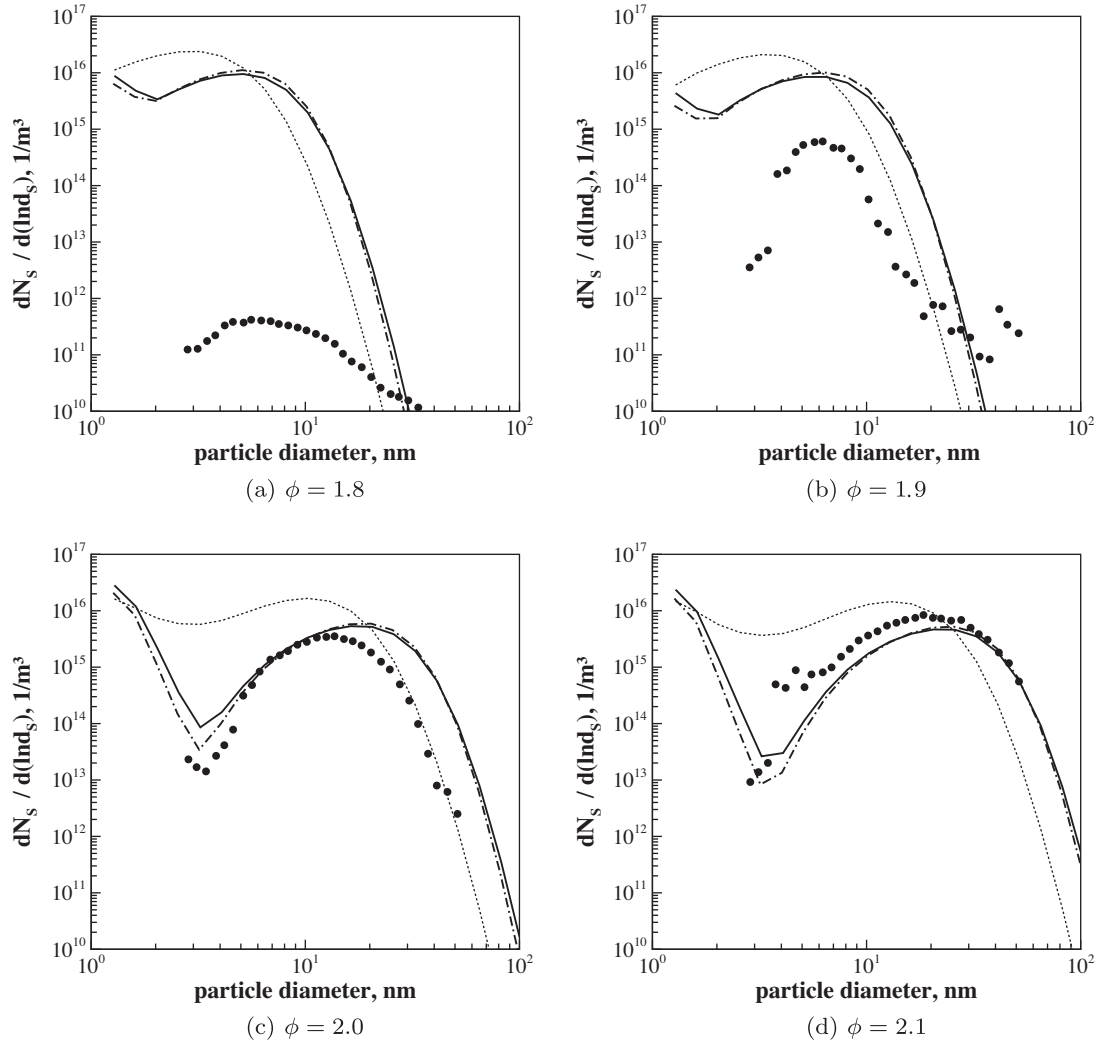

Fig. 5. Soot size distributions for different degrees of premixing ϕ. Symbols for measurements in the PFR by Manzello et al. [71] and lines for simulations, namely behind the WSR (dashed), in the PFR (solid), and in the PFR using an intra sectional distribution function constant in mass for soot particles (dash dot).

with smaller grid cells close to the burner, where the axial gradients are high. Because the heat flux from the flame to the burner surface is unknown, temperatures are not predicted but directly taken from the experiment. All further boundary conditions for the one-dimensional test case can be found in Table 6.

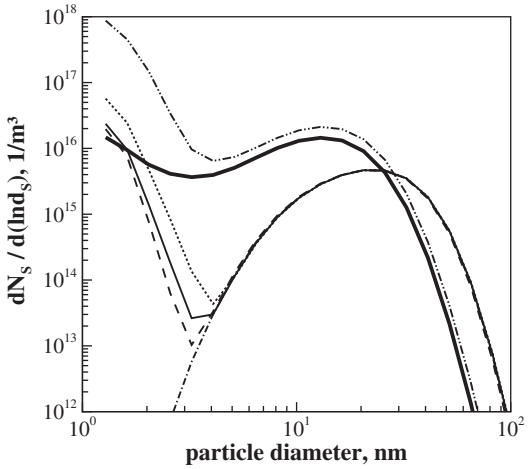

Fig. 6. Soot size distributions for ϕ = 2.1. Calculated profiles behind the WSR (thick solid) and in the PFR (thin solid) are compared to PFR-simulations without soot formation (dash dot), without C_2H_2 condensation (dash), without PAH soot collisions (dot), and without soot coagulation (dash dot dot).

Calculated soot volume fractions for the ethylene flames (flames 1–6) are compared with measurements in Fig. 7. Except for flame 2, very good agreement can be observed showing deviations in final soot volume fraction smaller than a factor two. Soot volume fractions for flame 2, however, are overpredicted by a factor 4. One reason for this strong deviation might be the

Table 6
Boundary conditions for laminar premixed flames studied by Tsurikov et al. [73].

Case	Fuel	Pressure (bar)	ϕ	u (m/s)
Flame 1	C_2H_4	1.0	2.30	0.073
Flame 2	C_2H_4	1.0	2.50	0.073
Flame 3	C_2H_4	3.0	2.30	0.248
Flame 4	C_2H_4	3.0	2.50	0.250
Flame 5	C_2H_4	5.0	2.05	0.221
Flame 6	C_2H_4	5.0	2.40	0.213
Flame 7	C_3H_6	1.0	2.23	0.049
Flame 8	C_3H_6	1.0	2.46	0.049
Flame 9	C_3H_6	3.0	2.10	0.038
Flame 10	C_3H_6	3.0	2.30	0.038
Flame 11	C_3H_6	5.0	2.30	0.023
Flame 12	C_7H_8	1.0	1.91	0.022
Flame 13	C_7H_8	1.5	1.88	0.021
Flame 14	C_7H_8	3.0	1.75	0.012

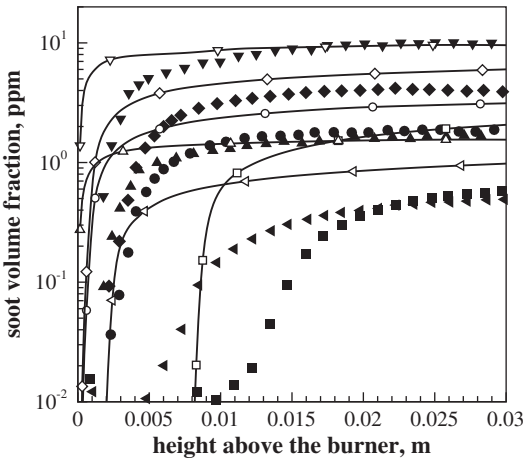

Fig. 7. Profiles of soot volume fraction for laminar premixed ethylene/air flames. Experimental data by Tsurikov et al. [73] (filled symbols) and simulations (lines with open symbols). Different symbols for flame 1 (left triangle), 2 (square), 3 (circle), 4 (diamond), 5 (delta), and 6 (gradient).

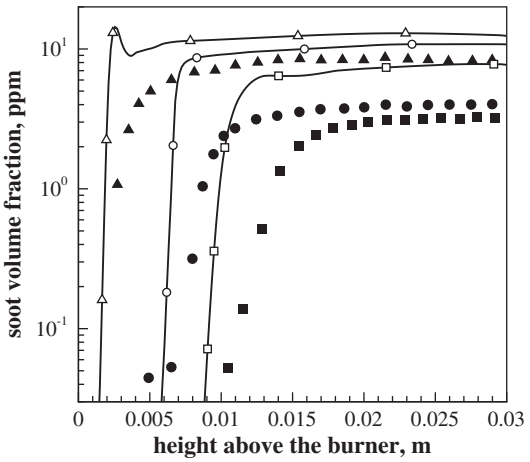

Fig. 9. Profiles of soot volume fraction for laminar premixed toluene/air flames. Experimental data by Tsurikov et al. [73] (filled symbols) and simulations (lines with open symbols). Different symbols for flame 12 (square), 13 (circle), and 14 (triangle).

"unflatness" of flame 2 in the experiment, which can be derived from the LII image of the experimental data [73]. If the radial gradients in this flame are no longer negligible and fluxes in radial direction need to be taken into account, one-dimensional calculations become erroneous.

In Fig. 8 predictions and measurements of soot volume fractions for the propylene flames (flames 7–11) are shown. Except for flame 9, good agreement can be observed showing deviations in final soot volume fraction smaller than a factor two. According to the experimental data a reduction of the premixing ratio from $\phi = 2.3$ (flame 10) to $\phi = 2.1$ (flame 9) leads to a fivefold reduction in soot volume fraction, which could not be reproduced by the model. A general deficiency of the model for rich fuel/air mixtures can be excluded though because flame 11 shows excellent agreement between simulations and measurements.

Soot predictions for the toluene flames (flames 12–14) are plotted in Fig. 9 along with the experimental data. Good agreement is found in all three cases but the deviations are greater than for the ethylene and propylene flames. Soot volume fractions are overpredicted by a factor of 2–3 but the trend in soot rise for rising pressures is very well predicted.

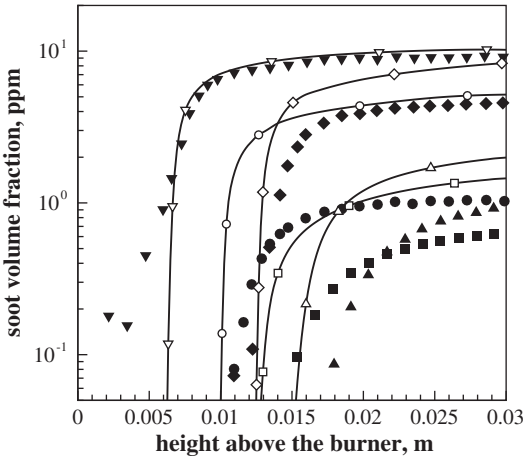

Fig. 8. Profiles of soot volume fraction for laminar premixed propylene/air flames. Experimental data by Tsurikov et al. [73] (filled symbols) and simulations (lines with open symbols). Different symbols for flame 7 (square), 8 (delta), 9 (circle), 10 (diamond), and 11 (gradient).

In summary the qualitative behavior of soot production is well reproduced for 12 out of 14 premixed flames studied in the work by Tsurikov et al. [73]. In most cases soot levels tend to be overpredicted and the onset of soot appears slightly too early. It is uncertain, if this is caused by difficulties in predicting major soot precursor species, since no measurements are available for acetylene, benzene, or even toluene. Another reason could be the PAH submodel because the reversibility of PAH reactions, which is only partially accounted for, might be responsible for the delayed onset of soot in the experiment. However, the predicted dependence of maximum soot volume fraction on pressure and premixing ratio is in good accordance with the experimental data.

3.3. Non-premixed laminar ethylene jet flames

Santoro et al. [74] studied the sooting behavior of non-premixed laminar jet flames. Their burner consisted of an 11.1 mm inner diameter fuel nozzle surrounded by a 101.6 mm outer air passage and extending 4 mm beyond the exit plane of the air passage. In order to shield the flame from the environment, it was enclosed by a 405 mm brass cylinder.

Calculations of Santoro's "flame 2" have been performed because a large amount of experimental data is available for this test case, which has often been cited and reproduced in the past by different authors [75–78]. In addition, also Santoro's "flame 4" has been simulated in order to evaluate model predictions for slightly smoking flames. The boundary conditions of these flames are summarized in Table 7.

In Fig. 10 the computed axial profile of soot volume fraction is compared with the experimental data by Santoro et al. [74], McEnally et al. [75], and Köylü et al. [76]. The deviation between the different experimental data in maximum soot volume fraction of more than 40% reflects the high uncertainties of soot volume fraction measurements for this test case. Hence, with regard to this uncertainty, excellent agreement between simulation and measurements is achieved.

Table 7
Boundary conditions for two laminar non-premixed jet flames studied by Santoro et al. [74].

Case	Fuel	Pressure (bar)	u_{fuel} (m/s)	u_{air} (m/s)
Flame 2	C_2H_4	1.0	3.98	8.9
Flame 4	C_2H_4	1.0	5.05	13.3

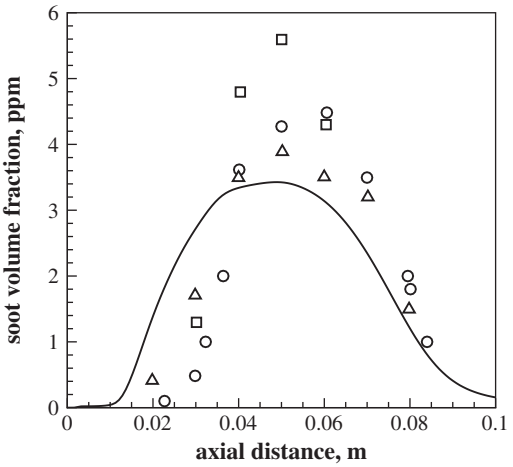

Fig. 10. Soot volume fraction profile along the center line for Santoro's flame 2. Simulation (line) along with experimental data by Santoro et al. [74] (circle), McEnally et al. [75] (square), and Köylü et al. [76] (triangle).

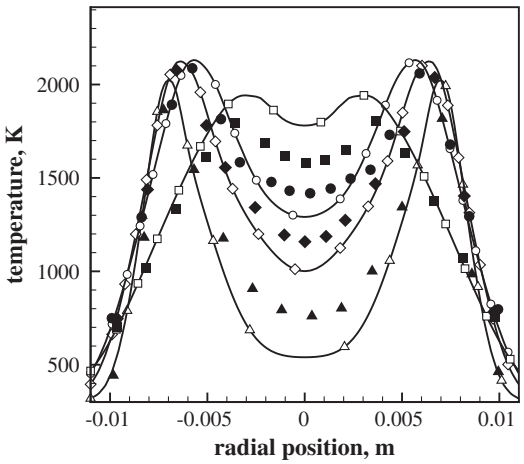

Fig. 12. Radial temperature profiles for Santoro's flame 2. Experimental data by McEnally et al. [75] (filled symbols) and simulations (lines with open symbols). Different symbols for heights above the burner: 3 mm (triangle), 10 mm (diamond), 20 mm (circle), and 50 mm (square).

In Fig. 11 radial profiles of soot volume fraction are compared with experimental data by McEnally et al. [75]. Whereas good agreement is found for positions 10 mm and 50 mm above the burner, at 30 mm soot volume fractions are overpredicted by more than a factor of two. However, the radial position of the peak in soot volume fraction is well predicted and soot is found in the same regions as in the experiment.

For flame 2 Santoro et al. [74] also performed temperature measurements using thermocouples. In Fig. 12 radial profiles from the experiment are compared to the simulation. Although the flame front is very well resolved for all heights above the burner, along the axis deviations seem to be rather high. However, especially close to the burner thermocouple measurements on the centerline of the flame are known to experience high measurement uncertainties. In contrast the overprediction of temperatures further downstream at 50 mm above the burner is due to the underprediction of soot in these regions. Here, the underpredicted soot levels lead to a lower heat radiation flux and in consequence to higher temperature levels.

Santoro pointed out that the oxidation rates of soot appear to be directly controlled by the local temperature, which is strongly affected by radiative heat transfer. Therefore, heat transfer has to be modeled with care in order to correctly predict soot in the downstream region of the flame, where soot oxidation reactions become relevant. Especially in the case of smoking flames soot oxidation is very sensitive to heat radiation because soot particles are transported to oxygen-rich regions in high concentrations. In this regard integrated soot volume fractions along the axis have been calculated for flame 2 and 4. The simulations have been conducted using the original heat radiation flux and one being twice as big. The computations are compared with the experimental data in Fig. 13. In case of flame 2 the original heat radiation flux seems adequate, since good agreement with the experimental data is observed. A heat flux twice as big causes lower temperatures and an overprediction of soot towards the end of the flame due to reduced oxidation rates. In contrast, the soot concentrations in the downstream region of flame 4 cannot be reproduced with the original heat radiation model because oxidation rates are still too high. Only by doubling the heat flux, adequate model predictions are achieved. This demonstrates the high sensitivity of soot predictions with respect to the radiation model for strongly sooting flames.

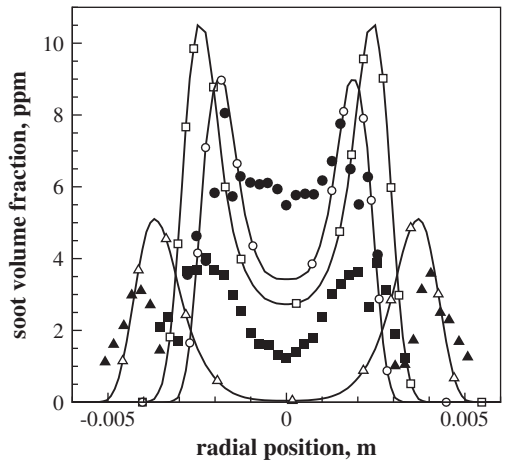

Fig. 11. Radial soot volume fraction profiles for Santoro's flame 2. Experimental data by McEnally et al. [75] (filled symbols) and simulations (lines with open symbols). Different symbols for heights above the burner: 10 mm (triangle), 30 mm (square), and 50 mm (circle).

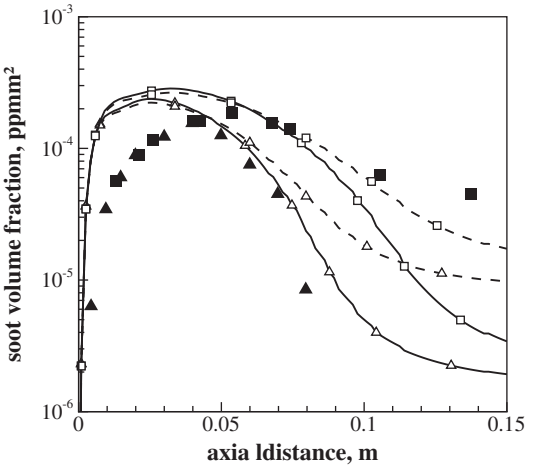

Fig. 13. Radially integrated soot volume fractions along the center line. Experimental data by Santoro et al. [74] (filled symbols), reference simulation (solid lines with open symbols), and simulations using a doubled heat flux (dashed lines with open symbols) for Santoro's flame 2 (triangle) and 4 (square).

3.4. Partially premixed laminar ethylene jet flames

McEnally and Pfefferle [79] performed experimental studies on a set of confined laminar partially premixed ethylene/air flames at different equivalence ratios $\phi = 3$, 4, 6, 12, 24, and ∞. The experimental data has been collected exclusively along the centerline of the flame. Selected species have been measured using probes as well as LIF. Temperatures have been determined with thermocouples and soot was captured by LII. All test cases have been simulated and good agreement with the measurements is observed. Representatively, only the cases $\phi = 3$, 6, and ∞ are discussed. Because of its minor concentration, Argon has been neglected leading to the boundary conditions given in Table 8.

As shown in Fig. 14, the calculated temperatures are in good agreement with the measurements. Also key species to the soot model such as acetylene and benzene are well predicted (see Figs. 15 and 16) for all three equivalence ratios. This agreement is a fundamental requirement in order to be able to evaluate the quality of the PAH and soot submodels as they strongly depend on these species.

In Fig. 17 profiles of soot volume fraction are presented. Good agreement with the experiment is found for all three premixings. The maximum deviation in peak soot volume fraction is within a factor of two. However, the region of high soot concentrations seems to be broader for the simulation. Reasons for the earlier soot onset might be found in an insufficient modeling of the reversibility of PAH reactions as mentioned before. Likewise, deficiencies in the gas phase reaction mechanism cannot be excluded. The later decline in soot volume fraction is certainly due to deviations in the oxidation process. However, the oxidation process is not solely a function of rate coefficients, which could be tuned but it is also a function of the involved gas phase species and the heat radiation model as shown before. Nevertheless, the general agreement is good, in particular regarding that no single parameter of the model has been tuned.

Table 8
Inflow conditions for McEnally's partially premixed flames. Units are m, s.

Case	Fuel (fully developed pipe flow)					Coflowing air		
	$\bar{u}$	$Y_{C_2H_4}$	Y_{O_2}	Y_{N_2}	T	u	Y_{O_2}	Y_{N_2}
$\phi = 3$	0.3579	0.1216	0.1403	0.7381	400			
$\phi = 6$	0.2639	0.1740	0.1004	0.7256	420	0.3317	0.23	0.77
$\phi = \infty$	0.1629	0.3059	0.0	0.6941	450			

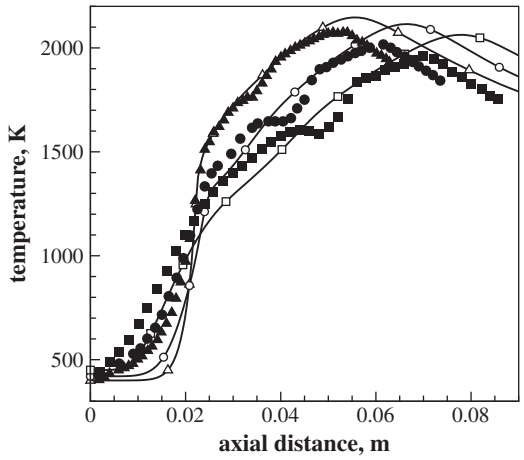

Fig. 14. Temperature profiles along the center line for the partially premixed flames by McEnally and Pfefferle [79]. Experimental data (filled symbols) and simulations (lines with open symbols). Different symbols for premixings $\phi = 3$ (triangle), $\phi = 6$ (circle), and $\phi = \infty$ (square).

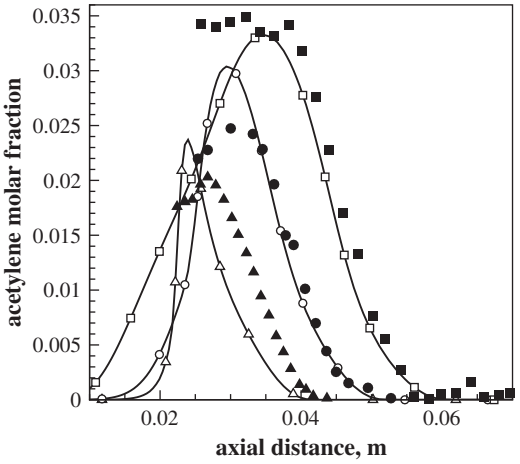

Fig. 15. Profiles of acetylene molar fraction along the center line for the partially premixed flames by McEnally and Pfefferle [79]. Experimental data (filled symbols) and simulations (lines with open symbols). Different symbols for premixings $\phi = 3$ (triangle), $\phi = 6$ (circle), and $\phi = \infty$ (square).

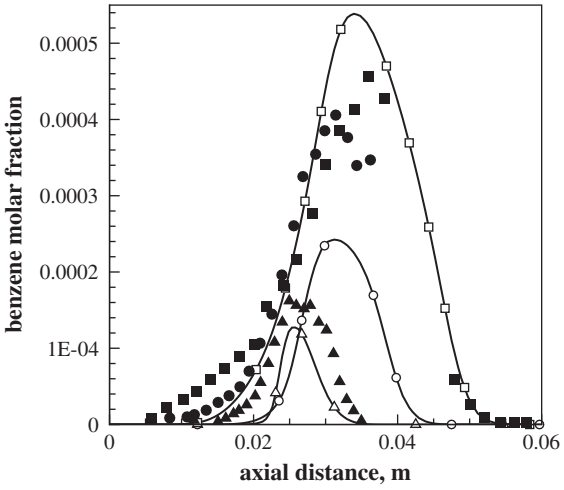

Fig. 16. Profiles of benzene molar fraction along the center line for the partially premixed flames by McEnally and Pfefferle [79]. Experimental data (filled symbols) and simulations (lines with open symbols). Different symbols for premixings $\phi = 3$ (triangle), $\phi = 6$ (circle), and $\phi = \infty$ (square).

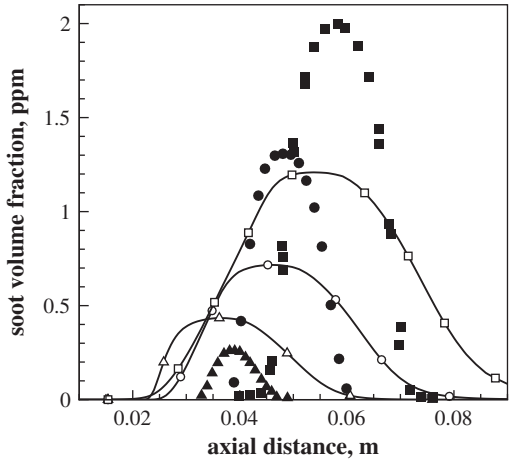

Fig. 17. Profiles of soot volume fraction along the center line for the partially premixed flames by McEnally and Pfefferle [79]. Experimental data (filled symbols) and simulations (lines with open symbols). Different symbols for premixings $\phi = 3$ (triangle), $\phi = 6$ (circle), and $\phi = \infty$ (square).

In Fig. 18 calculated soot size distributions at the axial position of maximum soot volume fraction are shown for all three premixings. Since smaller values of ϕ yield less particles for inception, soot growth and coagulation reactions are slower leading in turn to smaller particles. Although the maximum in number density is smaller for high values of ϕ, the integrated number densities are roughly on the same order of $10^{16}1/m^3$ for all three flames. However, when comparing these results, it should be kept in mind that for high values of ϕ the maximum soot concentrations are found in the flame wings while for higher premixings it is found on the axis of the flame [43].

The evolution of the soot size distribution along the center line is given in Fig. 19 for $\phi = 6$. Up to 4 cm above the burner soot inception clearly dominates the shape of the size distribution, which is reflected by the high concentration of small particles. At the point of maximum soot volume fraction soot inception is still present but coagulation dominates the process leading to a local maximum for bigger particles. Further downstream soot inception becomes negligible because the distribution function no longer peaks for smallest particles. At 5 cm above the burner the number concentration of the smallest particles even drops below $10^{12}1/m^3$ due to growth reactions (including coagulation). With increasing distance to the burner soot oxidation becomes more and more important, which manifests in the recovering of smallest particles at 6 and 7 cm above the burner. The shift of the distribution function from 7 to 8 cm above the burner reflects the final domination of oxidation reactions beyond the 7 cm position.

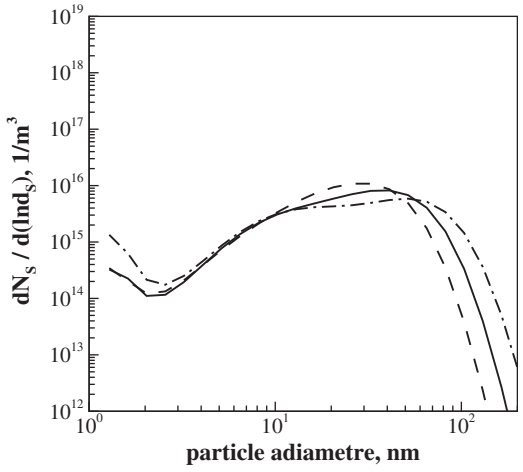

Fig. 18. Calculated soot size distributions at the axial position of maximum soot volume fraction for the partially premixed flames by McEnally and Pfefferle [79]. $\phi = 3$ (dash), $\phi = 6$ (solid), and $\phi = \infty$ (dash dot).

3.5. Non-premixed laminar kerosene jet flame

Moss and Aksit [11] studied the sooting behavior of a laminar non-premixed flame burning a kerosene surrogate consisting of volumetric 77% *n*-decane and 23% mesitylene. The nitrogen diluted fuel is injected by a 10 mm fuel tube, which is surrounded by coflowing air. The authors of the current work are not aware of a reliable kinetic mechanism in the literature for mesitylene which is valid between 300 and 2100 K. Thus, the kerosene surrogate mentioned by Slavinskaya [46] is used, which consists of volumetric 12% toluene (C_7H_8), 23% isooctane (C_8H_{18}), and 65% *n*-decane ($C_{10}H_{22}$). All boundary conditions are summarized in Table 9.

In Fig. 20 radial profiles of the soot volume fraction are shown. While at 15 mm the model yields higher values than the measurements, for positions 30 mm and 45 mm they are smaller. The deviation in maximum soot volume fraction, however, is always within a factor 2 except for the 15 mm position, where it is 2.4. At all three positions the model predicts the radial peak in soot volume fraction roughly 20% closer to the center line. Furthermore, the evolution of soot formation seems to be faster in case of the simulation, which manifests in higher soot volume fractions at low heights above the burner and in an earlier decline further downstream. However, the general agreement between simulation and experimental data is very promising. Moreover, it has to be kept in mind that different kerosene surrogates are used. The higher soot levels in the experiment at the axial positions 30 mm and 45 mm above the burner might be explained by a higher amount of aromatic

Table 9
Boundary conditions for the laminar non-premixed kerosene surrogate jet flame by Moss and Aksit [11].

Fuel mass fractions				Flow properties			
C_7H_8	C_8H_{18}	$C_{10}H_{22}$	N_2	T_{fuel}	u_{fuel}	T_{air}	u_{air}
0.035	0.082	0.291	0.592	540 K	0.13 m/s	366 K	0.63 m/s

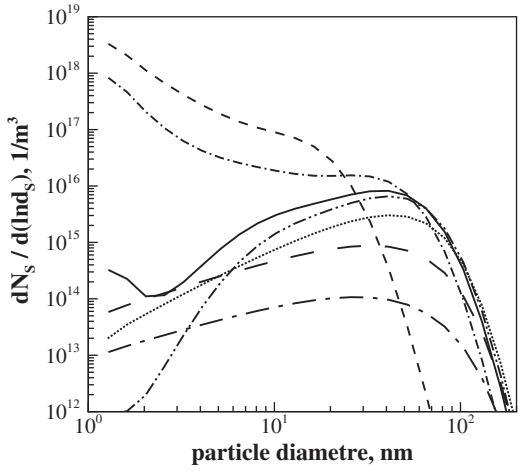

Fig. 19. Calculated soot size distributions for the $\phi = 6$ flame by McEnally and Pfefferle [79] at different axial positions, namely 3 (dash), 4 (dash dot), 5 (dash dot dot), 6 (dot), 7 (long dash), and 8 cm (long dash dot) above the burner. Solid line for position of maximum soot volume fraction.

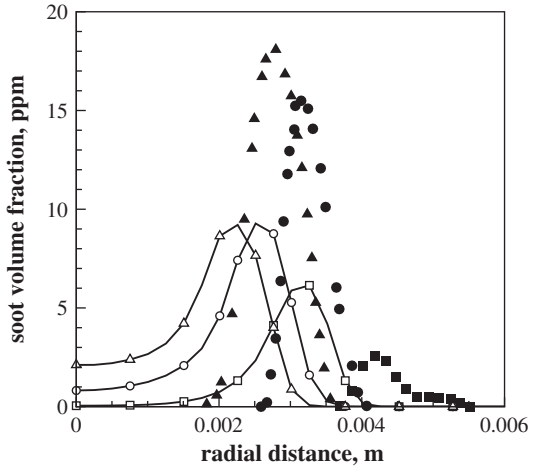

Fig. 20. Radial profiles of soot volume fraction for the laminar flame by Moss and Aksit [11]. Experimental data (filled symbols) and simulation (lines with open symbols). Different symbols for heights above the burner: 15 mm (square), 30 mm (circle), and 45 mm (triangle).

species (namely mesitylene) in the fuel, which can directly enter the path of PAH formation without having to decompose.

In Fig. 21 radial temperature profiles of the simulation are compared to the experimental data. Good agreement is found close to the burner while further downstream temperatures tend to be overpredicted especially close to the axis. The reason for this disagreement is uncertain and cannot solely be linked to the soot model because soot is overpredicted along the axis and should therefore lead to lower temperatures. Incertitudes in boundary conditions and the heat radiation model might be the cause, but also the fact that different fuels have been used.

In Section 2.3 the importance of the choice of soot enthalpies has been mentioned. In order to support this statement in the context of laminar flames, two further calculations have been performed with different assumptions for the enthalpy of soot particles. One simulation was conducted neglecting soot enthalpy and for the other one the mass specific enthalpy of the last PAH section was used. In addition a fourth calculation with a doubled heat radiation flux was realized. The results of all four simulations are presented in Fig. 22. The doubled heat flux clearly lowers the temperature in the sooting region resulting in a better agreement with the experimental data. In contrast, the zero enthalpy approach leads to a temperature rise, which is about three times higher than the temperature drop caused by the doubled heat flux. Using the mass specific enthalpy values of the last PAH section instead, lowers this temperature rise but it still remains significant. This clearly shows that for strongly sooting flames the choice of soot enthalpies can become as important as the choice of heat radiation model. In particular, the strong impact of uncertain soot enthalpy values may ruin the accuracy of a detailed and computationally expensive heat radiation model.

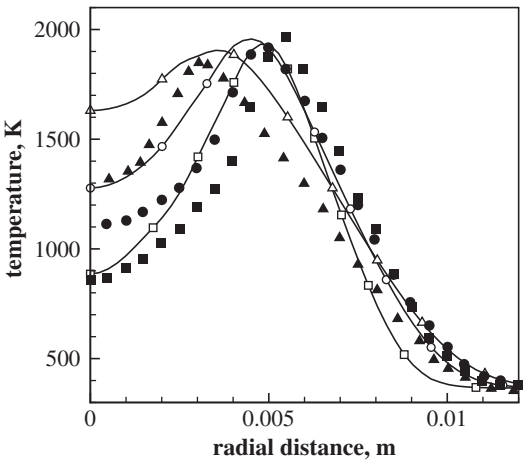

Fig. 21. Radial temperature profiles for the laminar flame by Moss and Aksit [11]. Experimental data (filled symbols) and simulation (lines with open symbols). Different symbols for heights above the burner: 15 mm (square), 30 mm (circle), and 45 mm (triangle).

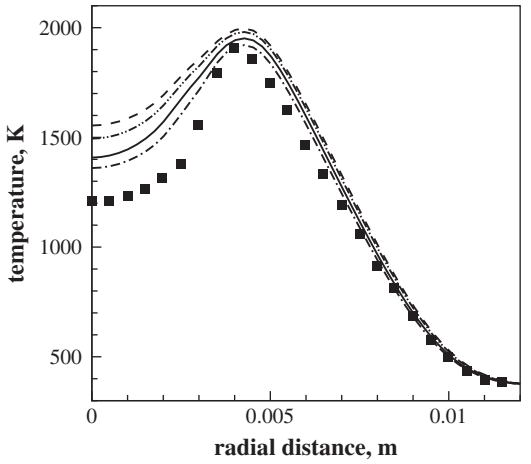

Fig. 22. Radial temperature profiles at 35 mm above the burner for the laminar flame by Moss and Aksit [11]. Experimental data (symbols) and simulations (lines), namely reference calculation (solid), $h_s = 0$ (dash), $h_s = h_{PAH_2}$ (dash dot dot), and doubled heat flux (dash dot).

4. Conclusion

A soot model has been presented based on a relatively slim chemical kinetic mechanism for the gas phase and a skeletal sectional approach for soot and PAH species. Soot volume fractions are well predicted for premixed, non-premixed, and partially premixed laminar flames covering a variety of fuels. In particular, the dependence on premixing ratio and pressure has been well captured with a deviation from experimental data within a factor of two for most cases. Flames showing maximum soot volume fractions as small as 0.5 ppm and as big as 20 ppm are reproduced, which demonstrates the wide range of applicability of the model.

The impact of important soot sub mechanisms on the soot particle size distribution was investigated. It has been shown that the local minimum of bimodal particle size distributions is caused by the interaction of soot formation and coagulation reactions, one mechanism promoting small and the other big particles. For an axisymmetric partially premixed flame the calculated particle size distributions allowed to identify dominating mechanisms of the soot model at different heights above the burner along the axis of the flame.

Furthermore, the importance of the choice of soot enthalpy has been pointed out and the need for more accurate thermodynamic data has been addressed.

Moreover, the influence of radiated heat on soot oxidation rates has been shown. This emphasizes the need for accurate heat radiation models in order to improve soot predictions in the downstream region of strongly sooting flames.

Acknowledgments

This work has been financed by the German Aerospace Center (DLR). The authors wish to express their gratitude to Dr. N. Slavinskaya for her constant support and for providing the chemical mechanism of the gas phase, which was a key tool in the improvement of the soot model.

References

[1] T.R. Barfknecht, Prog. Energy Combust. Sci 9 (1983) 199–237.
[2] E. Jensen, O. Toon, Nucleation Atmos. Aerosols (1996) 848–851.
[3] A. Petzold, J. Ström, F. Schröder, B. Kärcher, Atmos. Res. 33 (1999) 2689–2698.
[4] D. Mauzerall, B. Sultan, N. Kim, D.F. Bradford, Atmos. Environ. 39 (2005) 2851–2866.
[5] C. Lee, Combust. Flame 24 (1975) 239–244.
[6] A. Lefebvre, Int. Symp. Combust. 12 (1969) 1247–1253.
[7] M. Nakamura, S. Koda, K. Akita, Int. Symp. Combust. 19 (1982) 1395–1401.
[8] I. Kennedy, Prog. Energy Combust. Sci. 23 (1997) 95–132.
[9] B. Magnussen, B. Hjertager, Int. Symp. Combust. 16 (1977) 719–729.
[10] J. Moss, C. Stewart, K. Young, Combust. Flame 101 (1995) 491–500.
[11] J. Moss, I. Aksit, Proc. Combust. Inst. 31 (2007) 3139–3146.
[12] Z. Wen, S. Yun, M. Thomson, M. Lightstone, Combust. Flame 135 (2003) 323–340.
[13] D. Carbonell, A. Oliva, C. Perez-Segarra, Combust. Flame 156 (2009) 621–632.
[14] G. Ma, J. Wen, M. Lightstone, M. Thomson, Combust. Sci. Technol. 177 (2005) 1567–1602.
[15] H. El-Asrag, T. Lu, C. Law, S. Menon, Combust. Flame 150 (2007) 108–126.
[16] C. Saji, C. Balaji, T. Sundararajan, Int. J. Heat Mass Transfer 51 (2008) 4287–4299.

[17] P. Lindstedt, Soot Formation in Combustion, Springer, 1994.
[18] Yunardi, R. Woolley, M. Fairweather, Combust. Flame 152 (2008) 360–376.
[19] M. Di Domenico, P. Gerlinger, M. Aigner, Combust. Flame 157 (2010) 246–258.
[20] A. D'Anna, J. Kent, Combust. Flame 152 (2008) 573–587.
[21] H. Richter, S. Granata, W. Green, J. Howard, Proc. Combust. Inst. 30 (2005) 1397–1405.
[22] S. Dworkin, Q. Zhang, M. Thomson, N. Slavinskaya, U. Riedel, Combust. Flame. 158 (2011) 1682–1695.
[23] T. Blacha, M.D. Domenico, P. Gerlinger, M. Aigner, Soot modeling in partially premixed C_2H_4/air flames, AIAA paper 2010-1516.
[24] K. Leung, R. Lindstedt, W. Jones, Combust. Flame 87 (1991) 289–305.
[25] B. Zamuner, F. Dupoirieux, Combust. Sci. Technol. 158 (2000) 407–438.
[26] H. Guo, G. Smallwood, Combust. Flame 149 (2007) 225–233.
[27] T. Blacha, M.D. Domenico, M. Rachner, P. Gerlinger, M. Aigner, Modeling of soot and nox in a full scale turbine engine combustor with detailed chemistry, ASME paper GT2011-45084.
[28] M. Di Domenico, Numerical simulations of soot formation in turbulent flows, Ph.D. thesis, Universität Stuttgart, Germany, 2008.
[29] M. Frenklach, S. Harris, J. Colloid Interface Sci. 118 (1987) 252–261.
[30] F. Mauss, Entwicklung eines kinetischen modells der russbildung mit schneller polymerisation, Ph.D. thesis, Rheinisch-Westfälische Technische Hochschule Aachen, 1998.
[31] M. Balthasar, F. Mauss, A. Knobel, M. Kraft, Combust. Flame 128 (2002) 395–409.
[32] O. Lignell, J. Chen, P. Smith, Combust. Flame 155 (2008) 316–333.
[33] R. Mehta, D. Haworth, M. Modest, Combust. Flame 157 (2010) 982–994.
[34] S. Hong, M. Wooldridge, H. Im, D. Assanis, H. Pitsch, Combust. Flame 14 (2005) 11–26.
[35] N. Morgan, M. Kraft, M. Balthasar, D. Wong, M. Frenklach, P. Mitchell, Proc. Combust. Inst. 31 (2007) 693–700.
[36] K. Netzell, H. Lehtiniemi, F. Mauss, Proc. Combust. Inst. 31 (2007) 667–674.
[37] J. Singh, R. Patterson, M. Kraft, H. Wang, Combust. Flame 145 (2006) 117–127.
[38] B. Zhao, Z. Yang, M. Johnston, H. Wang, A. Wexler, M. Balthasar, M. Kraft, Combust. Flame 133 (2003) 173–188.
[39] B. Zhao, Z. Yang, Z. Li, M. Johnston, H. Wang, Proc. Combust. Inst. 30 (2005) 1441–1448.
[40] D. Kronholm, Molecular weight growth pathways in fuel-rich combustion, Ph.D. thesis, Massachusetts Institute of Technology, 2000.
[41] M. Naydenova, Soot formation modeling during hydrocarbon pyrolysis and oxidation behind shock waves, Ph.D. thesis, Rupertus Carola University of Heidelberg, 2007.
[42] S. Mosbach, M. Celnik, A. Raj, M. Kraft, H. Zhang, S. Kubo, K.-O. Kim, Combust. Flame 156 (2009) 1156–1165.
[43] T. Blacha, M.D. Domenico, N. Slavinskaya, P. Gerlinger, M. Aigner, Modeling of soot size distributions in partially premixed C_2H_4/air flames, AIAA paper 2011-0414.
[44] N. Slavinskaya, O. Haidn, Reduced chemical model for high pressure methane combustion with pah formation, AIAA paper 2008-1012.
[45] N. Slavinskaya, P. Frank, Combust. Flame 156 (2009) 1705–1722.
[46] N. Slavinskaya, Skeletal mechanism for kerosene combustion with pah production, AIAA paper 2008-0992.
[47] T. Blacha, M.D. Domenico, M. Köhler, P. Gerlinger, M. Aigner, Soot modeling in a turbulent unconfined C_2H_4/air jet flame, AIAA paper 2011-0114.
[48] C. Pope, J. Howard, Aerosol Sci. Technol. 27 (1997) 73–94.
[49] J. Yu, R. Sumathi, W. Green, JACS 126 (2004) 12685–12700. ISSN: 0002-786.
[50] M.D. Domenico, P. Gerlinger, M. Aigner, Modeling soot formation in methane diffusion flames, AIAA paper 2006-1163.
[51] M. Frenklach, D. Clarya, W. Gardiner, J. Stein, S. Stein, Int. Symp. Combust. 20 (1985) 887–901.
[52] M. Frenklach, H. Wang, Int. Symp. Combust. 23 (1990) 1559–1566.
[53] M. Frenklach, Phys. Chem. Chem. Phys. 4 (2002) 2028–2037.
[54] S. Harris, I. Kennedy, Combust. Sci. Technol. 59 (1988) 443–454.
[55] J. Miller, Int. Symp. Combust. 23 (1991) 91–98.
[56] N.A. Fuchs, The Mechanics of Aerosols, Pergamon Press, Oxford, 1964.
[57] H. El-Asrag, S. Menon, Combust. Flame 156 (2009) 385–395.
[58] D. Hu, Modellierung und modellentwicklung der rußbildung bei hohem druck in vorgemischten verbrennungssystemen, Ph.D. thesis, Institute of Energy Technique, University of Stuttgart, Germany, 2002.
[59] D. McQuarrie, J. Simon, Physical Chemistry, A Molecular Approach, University Science Books, Sausalito, California, 1997.
[60] R. Patterson, M. Kraft, Combust. Flame 151 (2007) 160–172.
[61] A. D'Anna, J.H. Kent, Combust. Flame 144 (2006) 249–260.
[62] A. Emelianov, A. Eremin, H. Jander, H. Wagner, Proc. Combust. Inst. 33 (2011) 525–532.
[63] A. Burcat, Prof. Burcat's Thermodynamic Data, 2011. <http://garfield.chem.elte.hu/Burcat/burcat.html>.
[64] S. Friedlander, Smoke, Dust and Haze – Fundamentals of Aerosol Behaviour, John Wiley & Sons Inc., A Wiley-Interscience Publication, New York, 1977.
[65] L. Tablot, R. Cheng, R. Schefer, D. Willis, J. Fluid Mech. 101 (1980) 737–758.
[66] A. Messerer, R. Niessner, U. Pöschl, Aerosol Sci. 34 (2003) 1009–1021.
[67] A. Habibi, B. Merci, G. Heynderickx, Comput. Chem. Eng. 31 (2007) 1389–1406.
[68] M. Modest, Radiative Heat Transfer, second ed., Acedemic, New York, 2003.
[69] M. Ravishankar, S. Mazumder, A. Kumar, J. Heat Transfer 132 (2010) 1–14.
[70] F. Liu, H. Guo, G. Smallwood, Ö. Gülder, J. Quant. Spectrosc. Radiat. Transfer 73 (2002) 409–421.
[71] S. Manzello, D. Lenhert, A. Yozgatligil, M. Donovan, G. Mulholland, M. Zachariah, W. Tsang, Proc. Combust. Inst. 31 (2007) 675–683.
[72] J. Bhatt, R. Lindstedt, Proc. Combust. Inst. 32 (2009) 713–720.
[73] M. Tsurikov, K. Geigle, V. Krüger, Y. Schneider-Kühnle, W. Strickner, R. Lückerath, R. Hadef, M. Aigner, Combust. Sci. Technol. 177 (2005) 1835–1862.
[74] R. Santoro, T. Yeh, J. Horvath, H. Semerjian, Combust. Sci. Technol. 53 (1987) 89–115.
[75] C. McEnally, Ü.Ö. Köylü, L. Pfefferle, D. Rosner, Combust. Flame 109 (1997) 701–720.
[76] Ü.Ö. Köylü, C. McEnally, D. Rosner, L. Pfefferle, Combust. Flame 110 (1997) 494–507.
[77] C. Megaridis, R. Dobbins, Combust. Sci. Technol. 66 (1989) 1–16.
[78] S. Iyer, T. Litzinger, S.-Y. Lee, R. Santoro, Combust. Flame 149 (2007) 206–216.
[79] C. McEnally, L. Pfefferle, Combust. Flame 121 (2000) 575–592.